

Article

Fracture and Damage Characteristics of Granite under Uniaxial Disturbance Loads

Botao Fei ¹, Gang Wang ^{2,3,*}, Xiping Li ³, Xiqi Liu ⁴  and Leibo Song ²

- ¹ School of Civil Engineering and Architecture, Wuhan University of Technology, Wuhan 430070, China; 2021000077@usx.edu.cn
- ² School of Civil Engineering, Shaoxing University, Shaoxing 312000, China; song_leibo@163.com
- ³ Hubei Key Laboratory of Roadway Bridge and Structure Engineering, Wuhan University of Technology, Wuhan 430070, China; xipingli@whut.edu.cn
- ⁴ Key Laboratory of Geotechnical and Structural Engineering Safety of Hubei Province, School of Civil Engineering, Wuhan University, Wuhan 430070, China; liu-xiqi@whu.edu.cn
- * Correspondence: gangw277842@whut.edu.cn; Tel.: +86-186-2432-6312

Abstract: To investigate the mechanical properties and damage characteristics of granite under frequent disturbance loads in the process of underground engineering construction, laboratory uniaxial compression tests were conducted on granite under combined dynamic and static loading conditions. The following conclusions were reached: (1) under a dynamic disturbance, the failure stress of granite grows gradually as the initial stress and disturbance load rise due to the coupling of damage and strain-rate effect; (2) the characteristic stresses of granite specimens grow with the increasing amplitude of disturbance $\Delta\sigma$ under the disturbing loads; with the same $\Delta\sigma$, the characteristic stresses show an increase trend with the increasing initial stress σ_m ; (3) the particle size distribution of rock fragments broken under the disturbance load follows the fractal law, and the fractal dimension F gradually enlarges with the growth of $\Delta\sigma$, indicative of an increased degree of fragmentation; and (4) the damage variable grows rapidly at first, then steadily, and, finally, shows a rapid growth trend again under the disturbance loads. The $\Delta\sigma$ significantly influences the number of cycles and rate of change of the damage variable during the steady increase. This research has certain theoretical significance and engineering guidance value for dynamic disaster recognition and control.

Keywords: granite; uniaxial disturbance load; characteristic stress; fractal dimension; damage



Citation: Fei, B.; Wang, G.; Li, X.; Liu, X.; Song, L. Fracture and Damage Characteristics of Granite under Uniaxial Disturbance Loads. *Buildings* **2022**, *12*, 1008. <https://doi.org/10.3390/buildings12071008>

Academic Editor: Elena Ferretti

Received: 18 June 2022

Accepted: 8 July 2022

Published: 13 July 2022

Publisher's Note: MDPI stays neutral with regard to jurisdictional claims in published maps and institutional affiliations.



Copyright: © 2022 by the authors. Licensee MDPI, Basel, Switzerland. This article is an open access article distributed under the terms and conditions of the Creative Commons Attribution (CC BY) license (<https://creativecommons.org/licenses/by/4.0/>).

1. Introduction

In geotechnical engineering and mine and rock mechanics, the stability of rocks is generally impaired by frequent disturbances. Especially in the underground excavation, the rock mass is subjected to the combination of high static load and frequent or cyclic external disturbances, among which the external disturbances include blasting, earthquake, mechanical vibration, etc. [1–4]. Under these conditions, the stress redistribution within a certain range caused by rock excavation and the external disturbance is the main cause of the frequent occurrence of disasters, such as rockbursts [5–7]. The strain rates for remote seismic and mechanical vibration loads range from 10^{-4} /s to 10^{-2} /s, which are quite different from the static loads' strain rates of less than 10^{-4} /s. The mechanical properties of rock vary greatly under high static stress and external disturbance [8,9]. Therefore, research on the mechanical properties and damage effect of rocks under disturbance loads is important for prevention of disasters and accidents in underground engineering operations.

In recent years, numerous scholars have conducted many experimental studies on the fracture characteristics of different types of rocks under cyclic loads. Zhu et al. [10] developed a disturbance electro-hydraulic servo triaxial test system. A series of disturbance relaxation tests on marble with different frequencies and amplitudes were carried out. The influence of cyclic disturbance parameters on the relaxation amplitude, relaxation rate, and

peak stress was analyzed. Ghasemi et al. [11] conducted monotonic and cyclic loading tests on gabbro specimens to study the evolution of micro-cracking therein under static and dynamic loading. The results indicated that compared with monotonic loading, cyclic loading facilitates the extension of micro-cracks earlier in the rock specimens, and the micro-cracks are longer. In order to study the deformation characteristics of brittle hard rock under cyclic disturbance loading, Cheng et al. [12] carried out cyclic loading and unloading tests at different loading and unloading rates, and analyzed the stress–strain curve’s modulus elasticity. Wang et al. [13] conducted multi-level compressive cyclic loading experiments to investigate the fracture evolution of naturally fractured granite using acoustic emission monitoring and post-test CT (Computer Tomography) scanning. Xu et al. [14] conducted a series of conventional uniaxial compression tests and cyclic loading tests on sandstone specimens and revealed that the maximum stress and the amplitude of the disturbance stress were the main factors influencing the fatigue life of sandstone. Meanwhile, the larger the maximum stress and the amplitude of the disturbance stress, the shorter the fatigue life of sandstone specimens. Manouchehrian et al. [15] established a tunnel numerical model and simulated the rock mass failure with static and dynamic loads. The results showed that the disturbance can accelerate the tunnel failure. Yang et al. [16] developed a loading method applicable to granite specimens under combined dynamic and static loading conditions. By using the method, they revealed changes in the mechanical properties of granite before and after loading and verified that the method is feasible through tests. Chen et al. [17] studied the influences of disturbance loads of different frequencies and amplitudes on the stress–strain characteristics, damage evolution, and failure modes of sandstone. The results show that the degree of fragmentation and ductility of the rock specimens both increase with the increasing frequency and amplitude of disturbance. Su et al. [18] conducted a true triaxial experimental study and found that under the action of low-frequency periodic disturbance, the threshold values of the axial static stress and amplitude of the disturbance load existed in a rockburst. Moreover, many scholars also have explored the mechanical properties of rocks under cyclic loading from the perspectives of acoustic emission (AE) characteristics, infrared thermography, and energy dissipation [19–29].

The aforementioned research has proved fruitful and is of important theoretical significance and guiding significance in engineering for those seeking to understand the failure mechanism of rocks under disturbance loads. However, most researchers focus on the deformation and mechanical characteristics of rocks under different initial stresses and disturbance loads, while seldom studying the fracture mechanism and damage characteristics of rocks under cyclic disturbance loads. Considering this, granite collected from the deep underground powerhouse in Shuangjiangkou Hydropower Station in Sichuan Province, China, was taken as the research object to conduct mechanical tests under low-frequency cyclic disturbances. On this basis, the characteristic stresses, fractal dimensions of fragments, and damage evolution of deeply buried rocks under dynamic disturbances were investigated, which has important theoretical significance and engineering guidance value for dynamic disaster recognition and control.

2. Materials and Methods

2.1. Test System and Specimen Preparation

The apparatus used in the test was an RTM electro-hydraulic servo test system developed by the Institute of Rock and Soil Mechanics, Chinese Academy of Sciences (Figure 1). Consisting mainly of a loading system, a measurement system, and a control system, the system can realize axial cyclic disturbance loading from 0 to 500 kN at frequencies from 0 to 20 Hz and can accurately, and in real-time, measure the mechanical properties of the specimens.

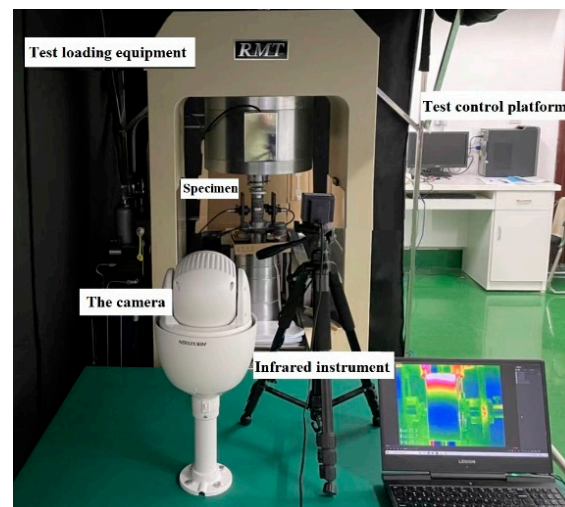


Figure 1. Test equipment.

The granite used in the test was collected from the underground powerhouse of Shuangjiangkou Hydropower Station in Sichuan Province, containing fine and uniform grains, tight textures, and few pre-existing cracks. With an intact structure, the rock specimens mainly comprise minerals including quartz (33%), potassium feldspar (26%), and plagioclase (36%), as well as accessory minerals (3%), such as black mica (Figure 2). After indoor coring, the granite was processed into standard cylinder specimens with a length of 100 mm and a diameter of 50 mm. The unevenness is less than 0.5 mm on both ends, and the tolerances on the diameter and height are within 0.3 mm. The two ends are perpendicular to the axis of the specimen, with the largest angle of deviation being no greater than 0.25° , which meets the requirements of the standard. The RMT electro-hydraulic servo test system was used to conduct uniaxial compression tests. The stress–strain curves are shown in Figure 3, and the basic parameters of the natural water content specimen (i.e., in the natural state) are shown in Table 1.

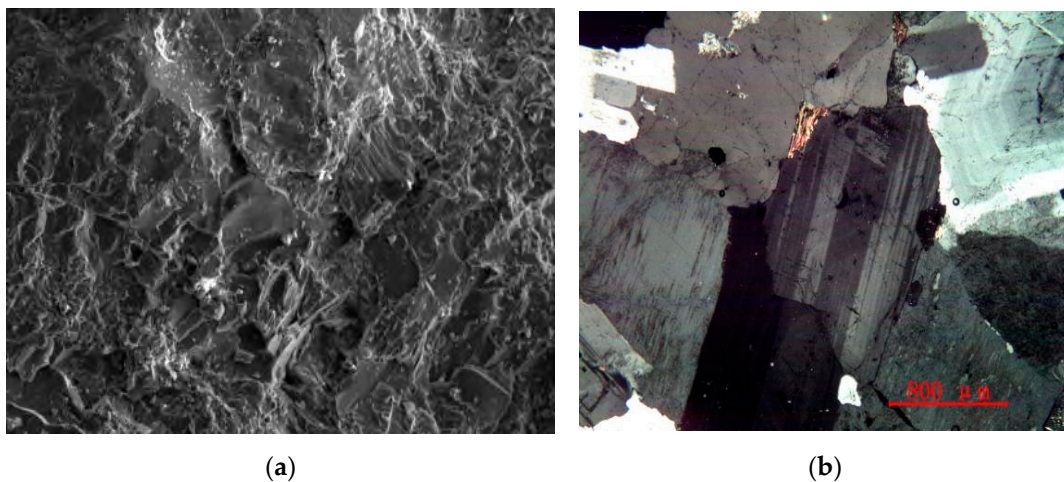


Figure 2. Mesoscopic characteristics of granite: (a) scanning electron microscopy micro-structures ($\times 500$); (b) polarized light microstructures.

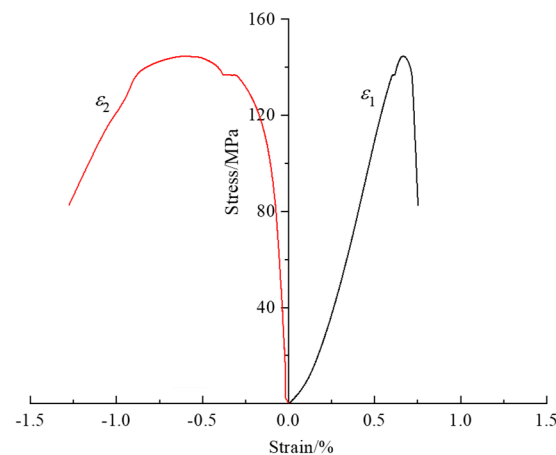


Figure 3. Stress–strain curves in the uniaxial compression test.

Table 1. Basic parameters of granite.

Serial Number	Uniaxial Compressive Strength/MPa	Elastic Modulus/GPa	Poisson Ratio	Density / $\text{kg} \times \text{m}^{-3}$	Wave Velocity / $\text{km} \times \text{s}^{-1}$
A1	142.32	32.15	0.21	2667	3.33
A2	144.84	31.29	0.21	2650	3.35
A3	147.36	30.43	0.21	2633	3.37

2.2. Test Schemes

Uniaxial dynamic and static combined loading was used in the tests (Figure 4). The stress control was used to apply axial static loads slowly on the specimens initially. After loading to the initial stress σ_m , cyclic disturbance loads with a sinusoidal waveform were applied. In the figure, T represents a loading cycle, and the upper and lower limits of disturbance loads are σ_{\max} and σ_{\min} , respectively, so the amplitude of disturbance is $\Delta\sigma = \sigma_{\max} - \sigma_{\min}$.

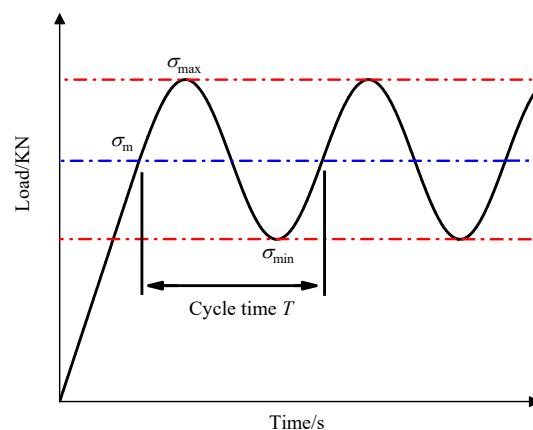


Figure 4. Cyclic disturbance loading.

The test schemes are listed in Table 2. At first, axial static loads are applied to the rock specimens at a rate of 1 kN/s to 60%, 70%, and 80% of the uniaxial compressive strength (UCS). The loading rate of 1 kN/s is based on the recommended range of test specification (Rock Test Code for SL/T 264-2020 for Water Conservancy and Hydropower Engineering) and the existing research results [30,31]. Afterwards, disturbance loads with amplitudes of 20, 30, and 40 MPa are applied, and the tests continue until failure of the specimens. In deep rock engineering, the dynamic disturbance loads are the main sources of

low-frequency cyclic disturbance loads [18]. These loads include stress waves propagating from a distant blasting source, seismic waves emitted from failure of a large volume of rocks near a cavern under excavation, vibration waves induced by mechanical drilling or low-frequency vibration of heavy equipment, and seismic waves triggered by natural earthquakes. Therefore, the cyclic disturbances frequency is set to 1 Hz for simulation of the conditions of deeply buried rock under different intensities of disturbance loads in an environment of certain static loads.

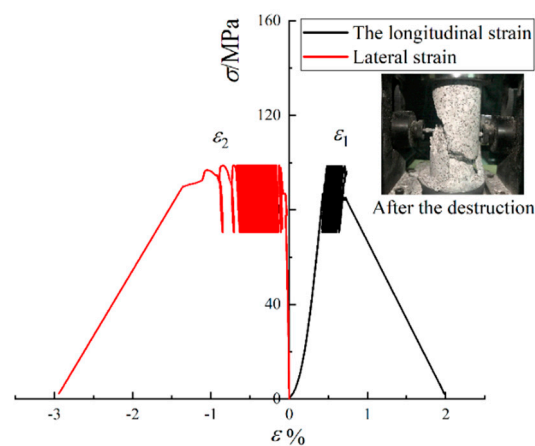
Table 2. Mechanical test schemes under cyclic dynamic disturbances.

Serial Number	σ_{\max} /MPa	Upper-Limit Stress Ratio/%	σ_{\min} /MPa	Lower-Limit Stress Ratio/%	σ_m /MPa	Average Stress Ratio/%	Amplitude /MPa
Gra60%-1	96.904	66.90	76.904	53.10	86.904	60	20
Gra60%-2	101.904	70.36	71.904	49.64	86.904	60	30
Gra60%-3	106.904	73.81	66.904	46.19	86.904	60	40
Gra70%-1	111.388	76.90	91.388	63.10	101.388	70	20
Gra70%-2	116.388	80.36	86.388	59.64	101.388	70	30
Gra70%-3	121.388	83.81	81.388	56.19	101.388	70	40
Gra80%-1	125.872	86.90	105.872	73.10	115.872	80	20
Gra80%-2	130.872	90.36	100.872	69.64	115.872	80	30
Gra80%-3	135.872	93.81	95.872	66.19	115.872	80	40

3. Results

3.1. Stress Analysis

Figures 5–7 show the stress–strain curves of various specimens under dynamic and static combined loading, in which ε_1 and ε_2 separately represent the longitudinal strain and transverse strain. It can be seen from the figures that the curve under the dynamic and static combined loading gradually shifts to the direction of increasing stress. Before failure of the rock, the stress–strain curves deviate significantly from the trajectory in historical cycles, and, finally, the rock is damaged at a certain point below the peak stress. Under the disturbance load, numerous shear fractures develop in the rock: these propagate and coalesce to form multiple shear failure planes that run through the specimen. In the context, macroscopic shear failure occurs to the rock. Because the stress on the rock specimen is relatively uniform in the loading process, the granite, as an elasto-brittle material, remains in the elastic deformation stage for a long time.



(a)

Figure 5. Cont.

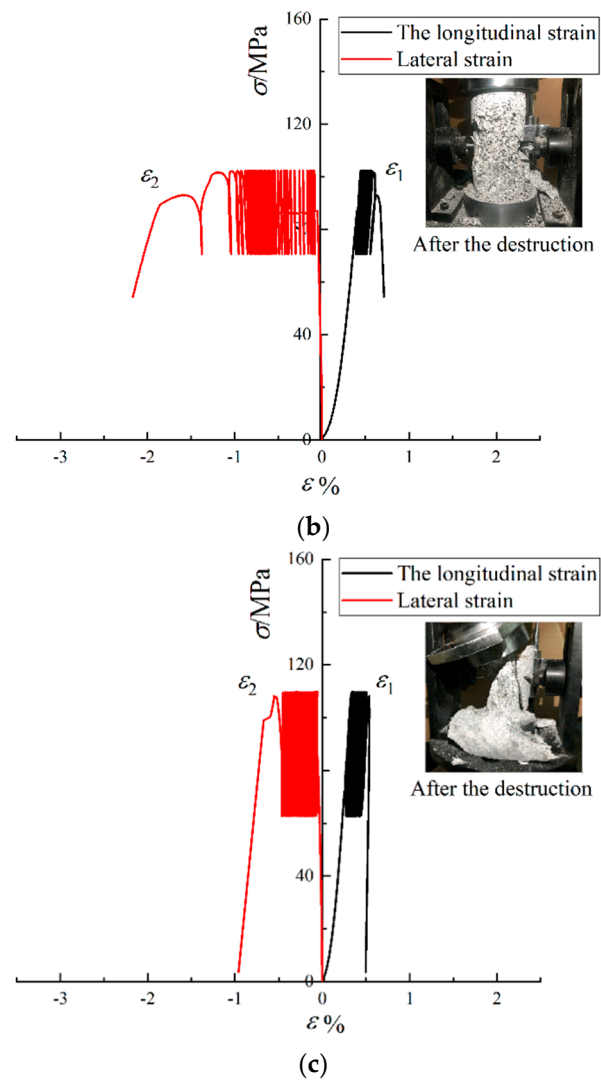


Figure 5. Stress–strain curves under 60% of the UCS: (a) Gra60%-1; (b) Gra60%-2; (c) Gra60%-3.

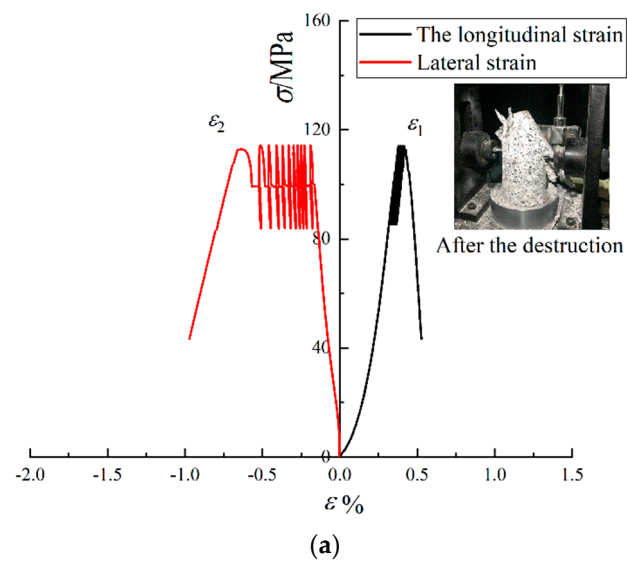


Figure 6. Cont.

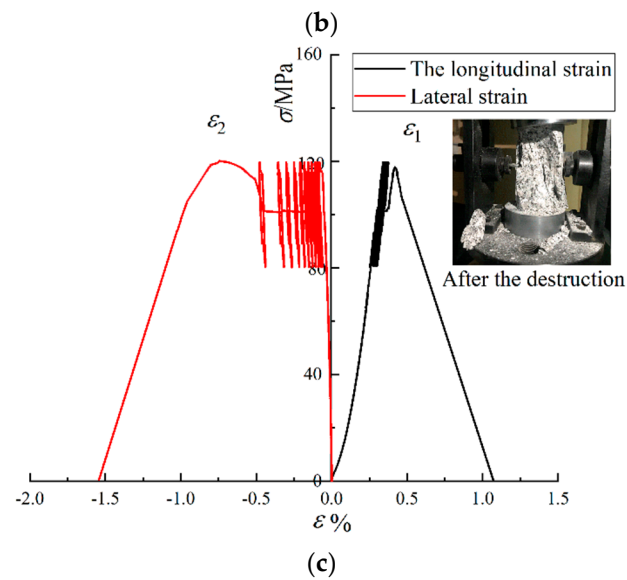
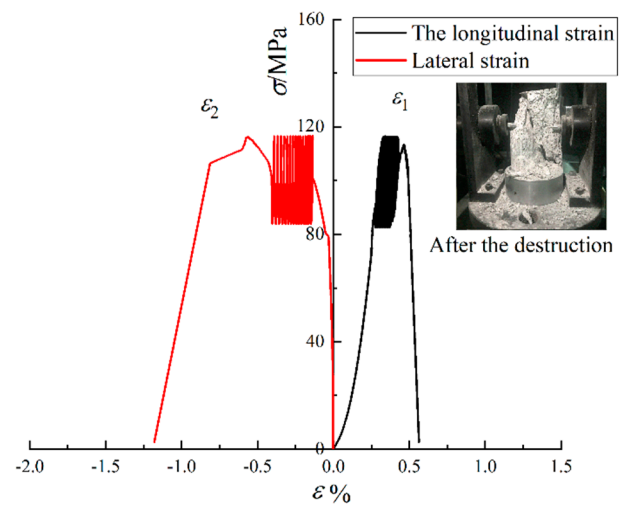


Figure 6. Stress–strain curves under 70% of the UCS: (a) Gra70%-1; (b) Gra70%-2; (c) Gra70%-3.

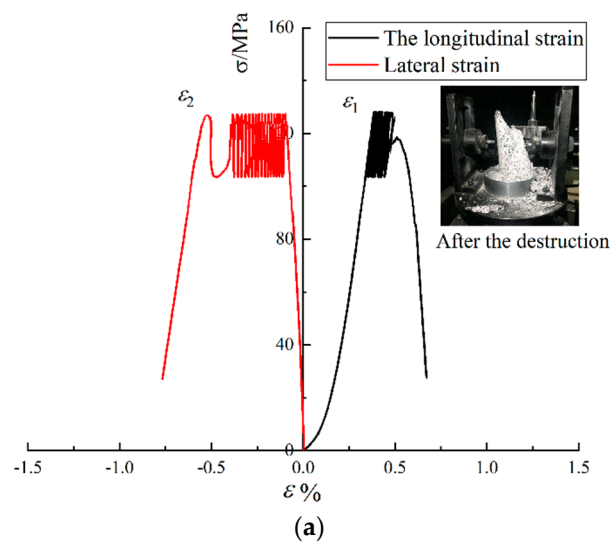


Figure 7. Cont.

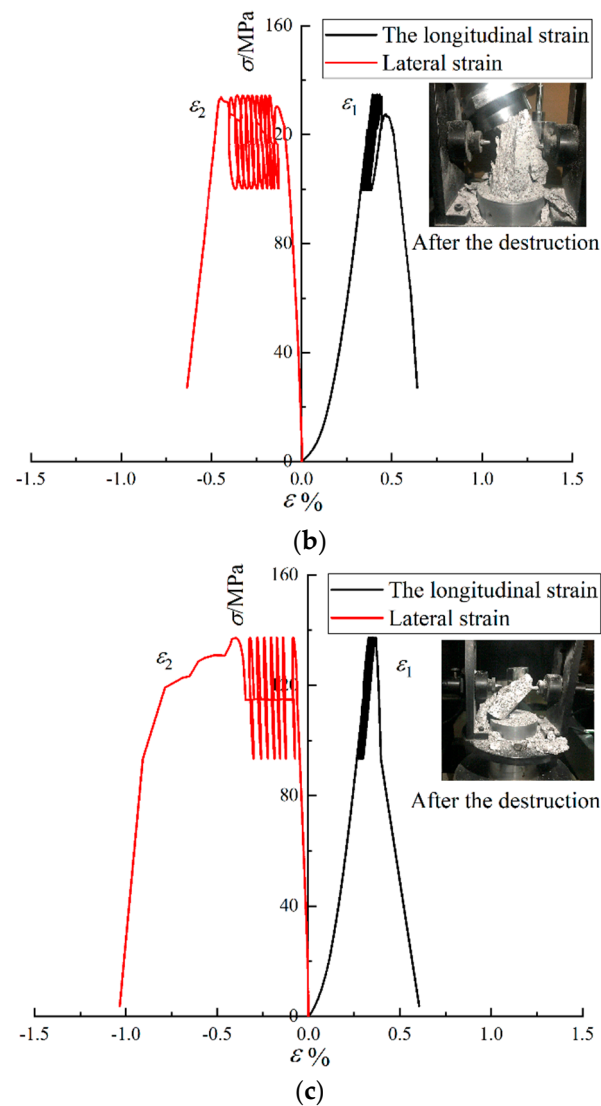


Figure 7. Stress–strain curves under 80% of the UCS: (a) Gra80%-1; (b) Gra80%-2; (c) Gra80%-3.

Table 3 lists the strengths of the rock specimens under different conditions. When the same initial axial static load σ_m is applied, the peak stress rises with the increasing amplitude of disturbance $\Delta\sigma$; if the amplitude $\Delta\sigma$ is the same, the peak stress shows an increasing trend with the increasing σ_m . Under uniaxial compression conditions, the specimen has a strength of 144.84 MPa. When the initial stress is 60% of the UCS, the peak stress separately decreased by 37.57%, 31.66%, and 27.33% with the growing amplitude of disturbance, compared with the UCS; when the initial stress is 70% of the UCS, the peak stress drops by 24.58%, 23.37%, and 18.39% as the amplitude of disturbance has an increment; and, with the increase in the initial stress to 80% of the UCS, the peak stress of the granite decreases by 20.47%, 12.17%, and 6.80% as the amplitude of disturbance grows.

Table 3. Strengths of granite specimens under different conditions.

σ_m Amplitude /MPa	60%			70%			80%		
	20	30	40	20	30	40	20	30	40
Strength /MPa	90.42	98.98	105.25	109.23	111.00	118.19	115.19	127.19	134.99

Under a low initial stress, the rock experiences many disturbances and then the route to failure, so it is more likely to be damaged, and, therefore, the failure load is low. If the initial stress is high, only a low number of disturbances are performed, so the degree of damage is low, and the specimen is damaged under higher stress. Under disturbances of a large amplitude, the failure load also enlarges because of strain-rate effects on the specimen.

The pre-peak section of the stress–strain curves of rocks during loading can be divided into four stages, i.e., an initial crack compaction stage, an elastic deformation stage, a stable crack propagation stage, and an unstable crack propagation stage [32,33], as illustrated in Figure 8. The four stages are characterized by the crack-closure stress σ_{cc} , crack-initiation stress σ_{ci} , crack-damage stress σ_{cd} , and peak stress σ_c . The volumetric strain of cracks is 0 in the initial state. Under axial stress, the pre-existing cracks inside the rock are gradually closed, so their volumetric strain increases. When the stress corresponding to the volumetric strain reaches σ_{cc} , pre-existing cracks are completely closed. Thereafter, the curve of the volumetric strain of cracks basically remains unchanged, indicating that no damage occurs inside the rock. If the stress is unloaded in this context, the rock can recover to its initial state, so the stage belongs to the elastic deformation stage. When the load is increased further, the volumetric strain associated with the cracks changes; new cracks are initiated within the specimen, and the stress corresponding to the point is the crack-initiation stress σ_{ci} . In the initial stage of the initiation of new cracks, there are a small number of new cracks, which develop slowly. As the volumetric strain ascends and reaches its maximum, the cracks enter a stage of rapid development, corresponding to the crack-damage stress σ_{cd} . When the load exceeds the peak stress σ_c , the specimen enters the unstable crack propagation stage.

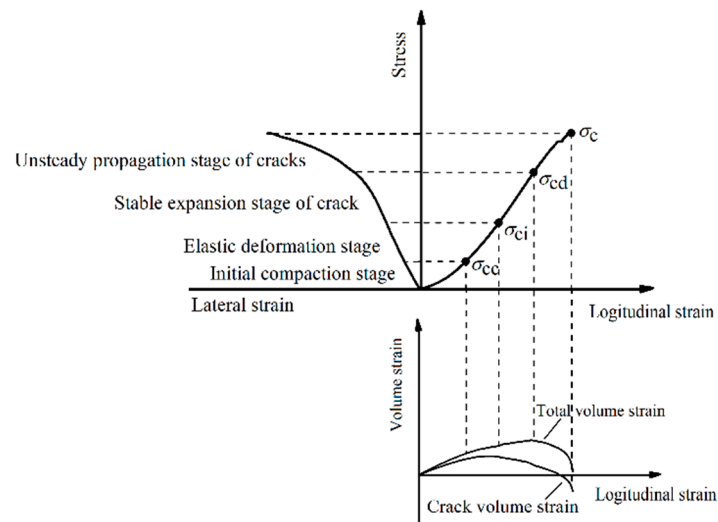


Figure 8. Division of damage evolution stages of the rock.

Existing methods used for calculating characteristic stresses mainly include strain measurement, AC measurement, and an approach based on the volumetric strain of cracks. Among these, the one based on the volumetric strain of cracks has been widely used due to its definite concept and convenience of determination [34,35]. The method mainly divides the volumetric strain of rocks into the elastic volumetric strain and volumetric strain of cracks. Under uniaxial compression, the volumetric strain of cracks, ε_v^c , in the rock can be calculated thus [36,37]:

$$\varepsilon_v^c = \varepsilon_v - \varepsilon_v^e = \varepsilon_v - \frac{1 - 2 \times \mu}{E} \times \sigma, \quad (1)$$

$$\varepsilon_v = \varepsilon_1 + 2 \times \varepsilon_2, \quad (2)$$

where ε_v and ε_v^e separately represent the volumetric strain of rocks and the elastic volumetric strain; ε_1 and ε_2 denote the longitudinal strain and transverse strain; μ represents the Poisson's ratio; and E represents the modulus of elasticity.

The volumetric strain of cracks calculated using Formulas (1) and (2) is displayed in Figures 9–11. Table 4 shows the normalization results of characteristic stresses (characteristic stresses/UCS) corresponding to each stage.

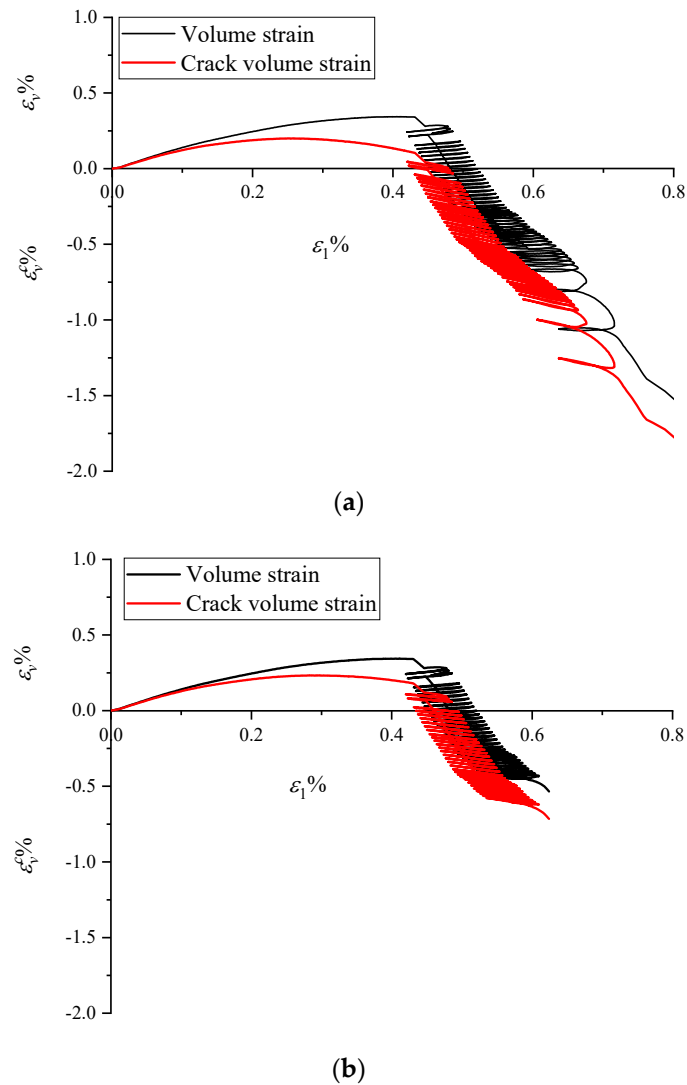


Figure 9. Cont.

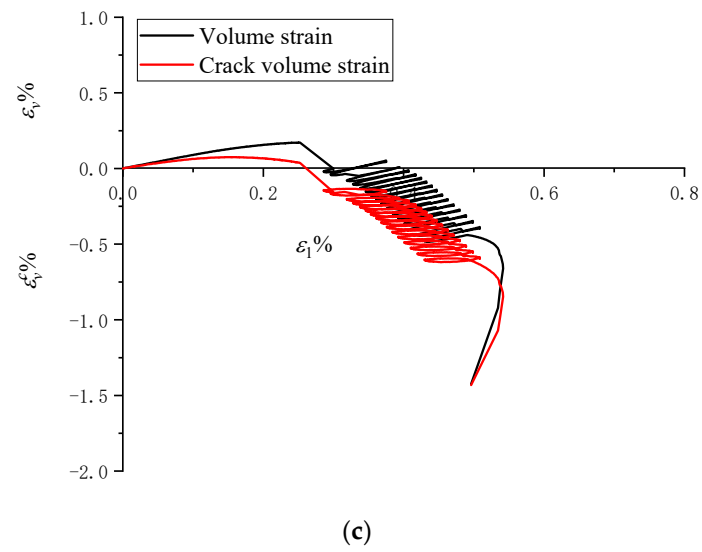


Figure 9. Volumetric strain of cracks under 60% of the UCS: (a) Gra60%-1; (b) Gra60%-2; (c) Gra60%-3.

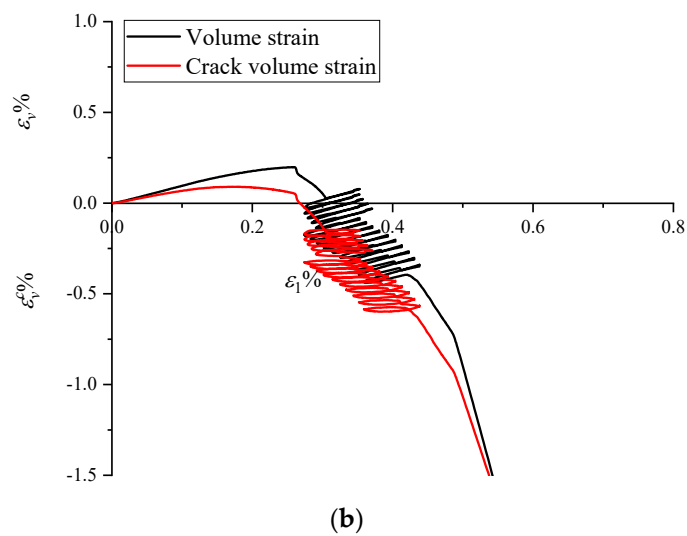
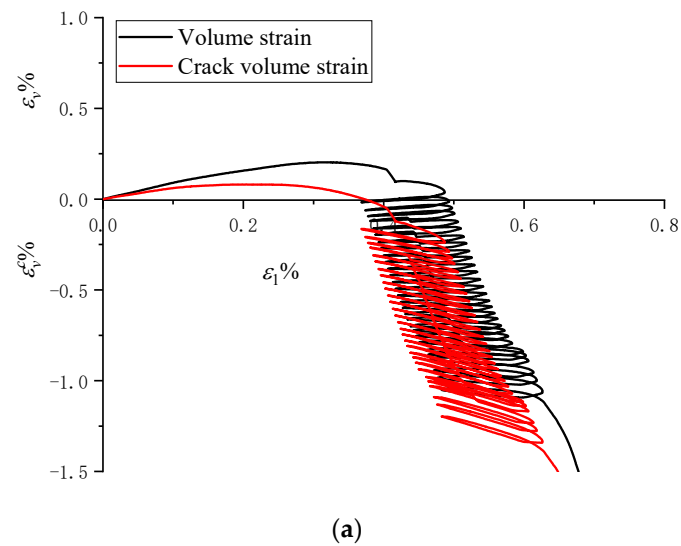


Figure 10. Cont.

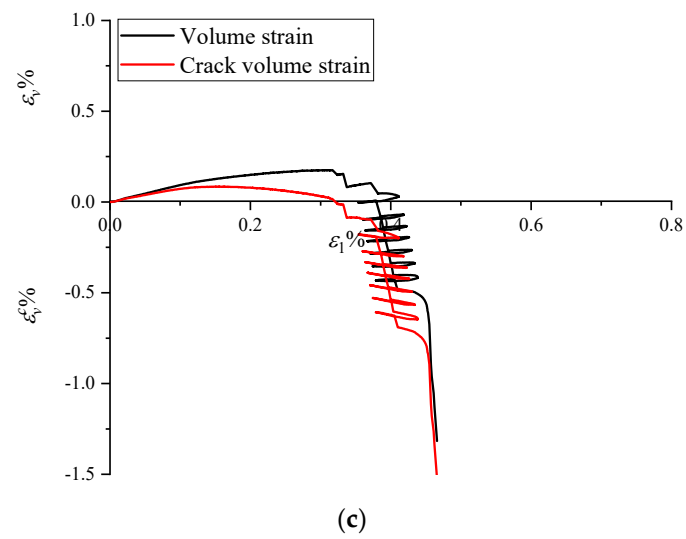


Figure 10. Volumetric strain of cracks under 70% of the UCS: (a) Gra70%-1; (b) Gra70%-2; (c) Gra70%-3.

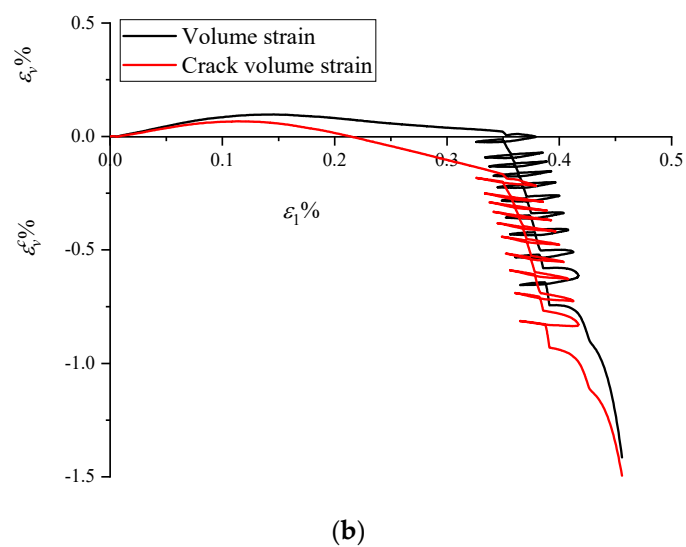
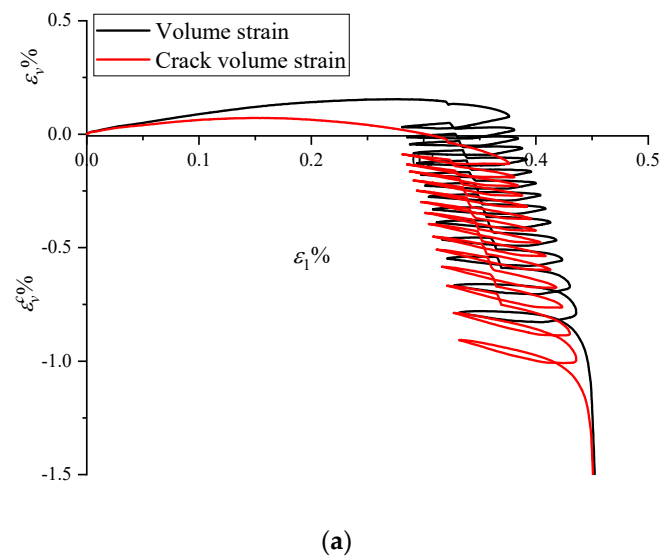


Figure 11. Cont.

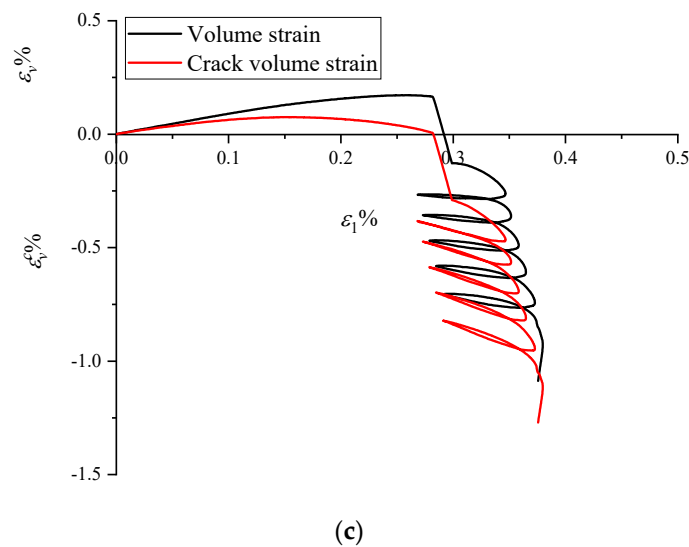


Figure 11. Volumetric strain of cracks under 80% of the UCS: (a) Gra80%-1; (b) Gra80%-2; (c) Gra80%-3.

Table 4. Values of characteristic stresses of rock specimens.

Serial Number	σ_{cc}/MPa	σ_{ci}/MPa	σ_{cd}/MPa	σ_c/MPa
Gra60%-1	0.065	0.148	0.279	0.409
Gra60%-2	0.069	0.172	0.292	0.450
Gra60%-3	0.071	0.179	0.301	0.470
Gra70%-1	0.066	0.168	0.281	0.414
Gra70%-2	0.072	0.176	0.300	0.458
Gra70%-3	0.084	0.186	0.302	0.471
Gra80%-1	0.067	0.173	0.296	0.438
Gra80%-2	0.080	0.188	0.303	0.465
Gra80%-3	0.095	0.202	0.338	0.477

As shown in Table 4, the characteristic stresses increase with the increasing amplitude of disturbance $\Delta\sigma$ when the same initial axial static load σ_m is applied; when $\Delta\sigma$ is same, the characteristic stresses show an increasing trend with the growth of σ_m .

The crack-initiation stress gradually increases under the same amplitude of disturbance but different static loading intensities. The crack-closure stress, crack-initiation stress, and crack-damage stress are separately 0.2, 0.4, and 0.7 times the peak stress. Combining with previous research [38,39], different types of rocks feature significantly different characteristic stresses. The difference is mainly related to factors including mineral compositions, internal structure, and petrogenic environment of rocks.

3.2. Failure Analysis

Many methods are available for quantitatively evaluating the degree of fragmentation of rocks, such as characteristic lumpiness, average lumpiness, and fractal dimension. Therein, fractal dimension has been extensively used in research into the degree of fragmentation of rocks due to its advantages, including its intuitive results and precise quantification.

3.2.1. Screening of Broken Rock Fragments

A GZS-300 standard vibrating sieve with aperture sizes from 0.05 to 45 mm is used to perform the screening tests for the broken rocks. Particle sizes of the fragments were graded into 10 levels from: 0.05 to 1, 1 to 5, 5 to 10, 10 to 15, 15 to 20, 20 to 25, 25 to 30, 30 to 35, 35 to 40, and 40 to 45 mm. In addition, the mass of the fragments remaining on the holes of the sieves was weighed and converted to the cumulative percentage of particles

below a given size. In this way, the particle size distribution of fragments of the granite under different amplitudes of disturbance is found (Figure 12).

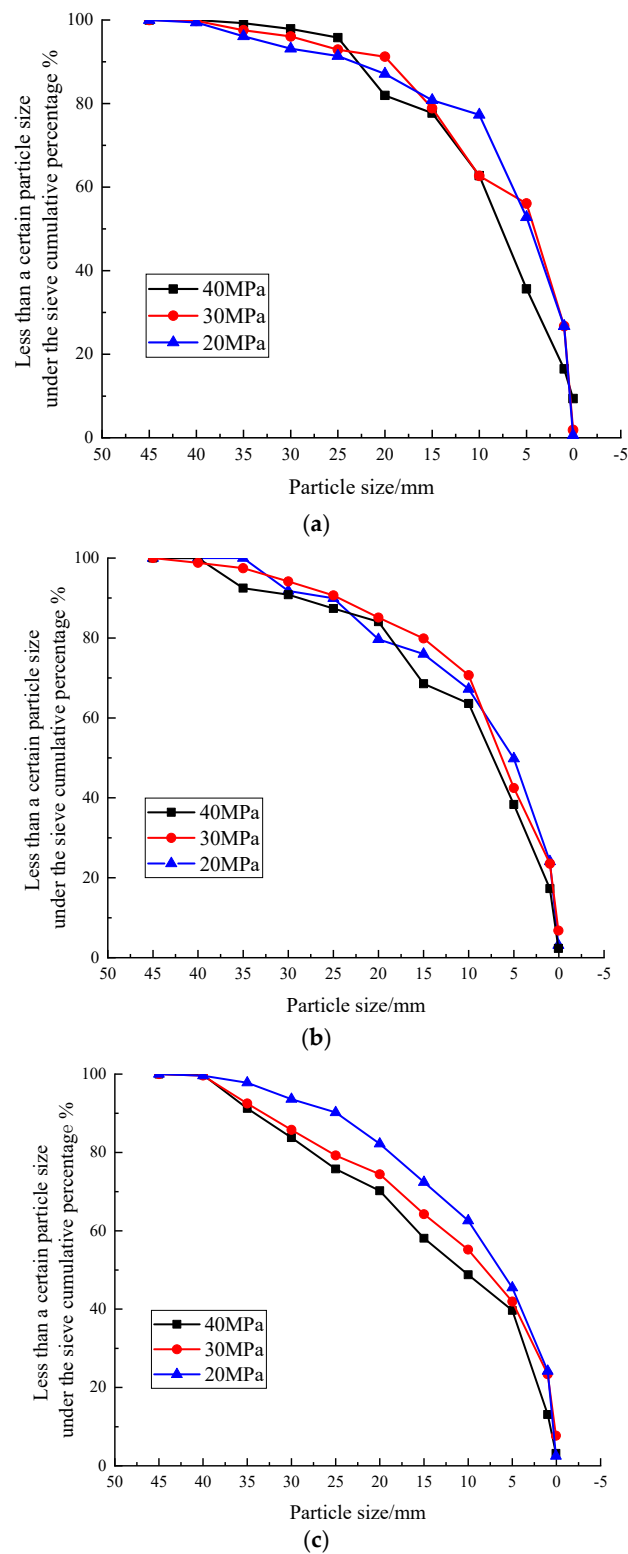


Figure 12. Particle size distributions of fragments under different amplitudes of disturbance: (a) Gra60%; (b) Gra70%; (c) Gra80%.

According to Figure 12, the effective size d_{10} , continuous size d_{30} , and control size d_{60} of fragments under different conditions are determined. The uniformity coefficient of

particle size distribution and the curvature coefficient of curves are calculated using the following formulas [40]:

$$C_u = \frac{d_{60}}{d_{10}}, \quad (3)$$

$$C_c = \frac{d_{30}^2}{d_{10} \cdot d_{60}}, \quad (4)$$

The uniformity coefficients of the particle size distribution of the fragments and the curvature coefficients are listed in Table 5: the uniformity coefficients C_u of rock specimens are all greater than five under different conditions, indicating that the particle sizes of fragments broken under the disturbance loads are distributed in a non-uniform manner. From rock specimen Gra70%-2, the curvature coefficient C_c is between one and three. Based on the evaluation criterion for particle size distribution, rock specimens Gra70%-2, Gra70%-3, Gra80%-1, Gra80%-2, and Gra80%-3 exhibit favorable particle size distributions after breaking.

Table 5. Uniformity coefficients and curvature coefficients.

Category	Gra60%			Gra70%			Gra80%		
	1	2	3	1	2	3	1	2	3
C_u	22.57	18.89	17.17	23.14	18.57	23.12	18.80	29.38	23.36
C_c	3.45	1.42	4.42	0.74	1.94	2.69	1.53	1.92	1.84

3.2.2. Calculation of Fractal Dimensions

The lumpiness distribution and particle size of broken rocks show favorable fractal characteristics. According to the fractal model for particle size distribution of rock fragments established by Mandelbrot et al. [41], the fractal dimension F is calculated based on the mass–frequency relation revealed in the screening tests. The equation for distribution of rock fragments generated under cyclic disturbance loads is expressed as follows [41]:

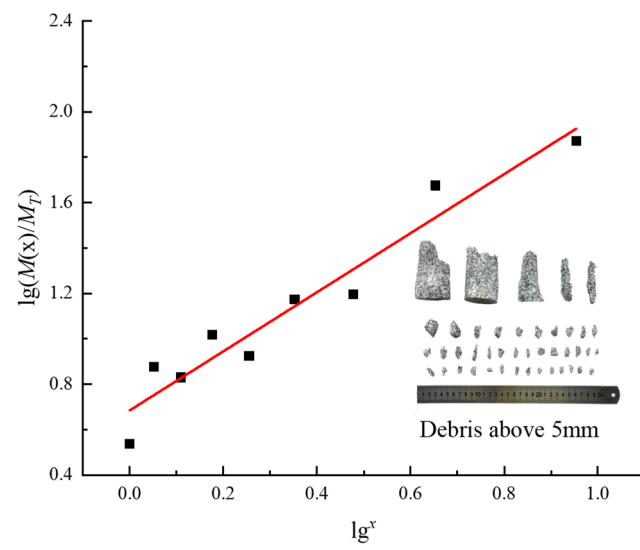
$$\frac{M(x)}{M_T} = \left(\frac{x}{x_m} \right)^{3-F}, \quad (5)$$

Taking logarithms of both sides of the above equation, gives

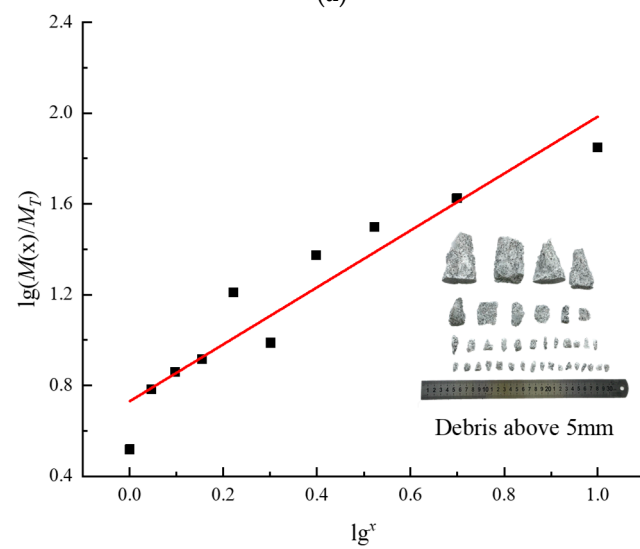
$$\lg \left(\frac{M(x)}{M_T} \right) = (3 - F) \times \lg \left(\frac{x}{x_m} \right), \quad (6)$$

where M_T and $M(x)$ represent the total mass of fragments and cumulative mass of fragments under sieves; x_m and x denote the maximum particle size and the particle size of fragments; and F is the fractal dimension.

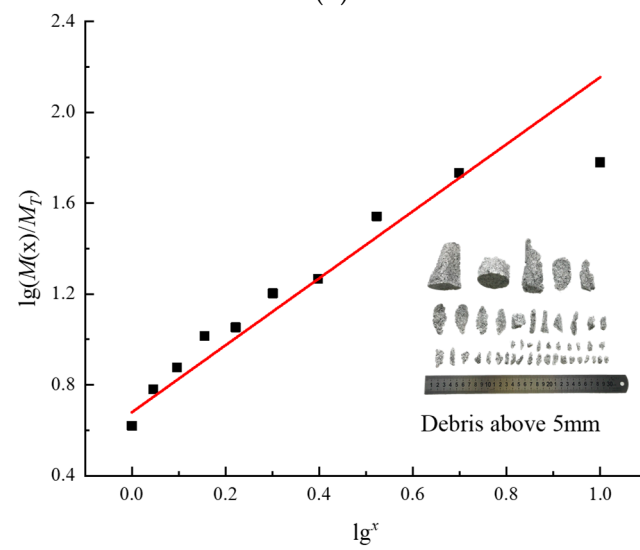
Figures 13–15 display the linearly fitted lines of $\log(M(x)/M_T)$ – $\log x$ scatter plots corresponding to different initial static loads σ_m . The fitted lines have a slope of $(3-F)$, so the fractal dimension F can be calculated. The fitting results indicate that the cumulative percentage of particles under sieves (by mass) has a favorable linear correlation with the sieve hole size in double logarithm coordinates. This suggests that the fractal dimension can be used to quantitatively characterize the degree of fragmentation of rock specimens.



(a)



(b)



(c)

Figure 13. The $\log(M(x)/M_T)$ - $\log x$ lines of rocks under 60% of the UCS: (a) 20 MPa; (b) 30 MPa; (c) 40 MPa.

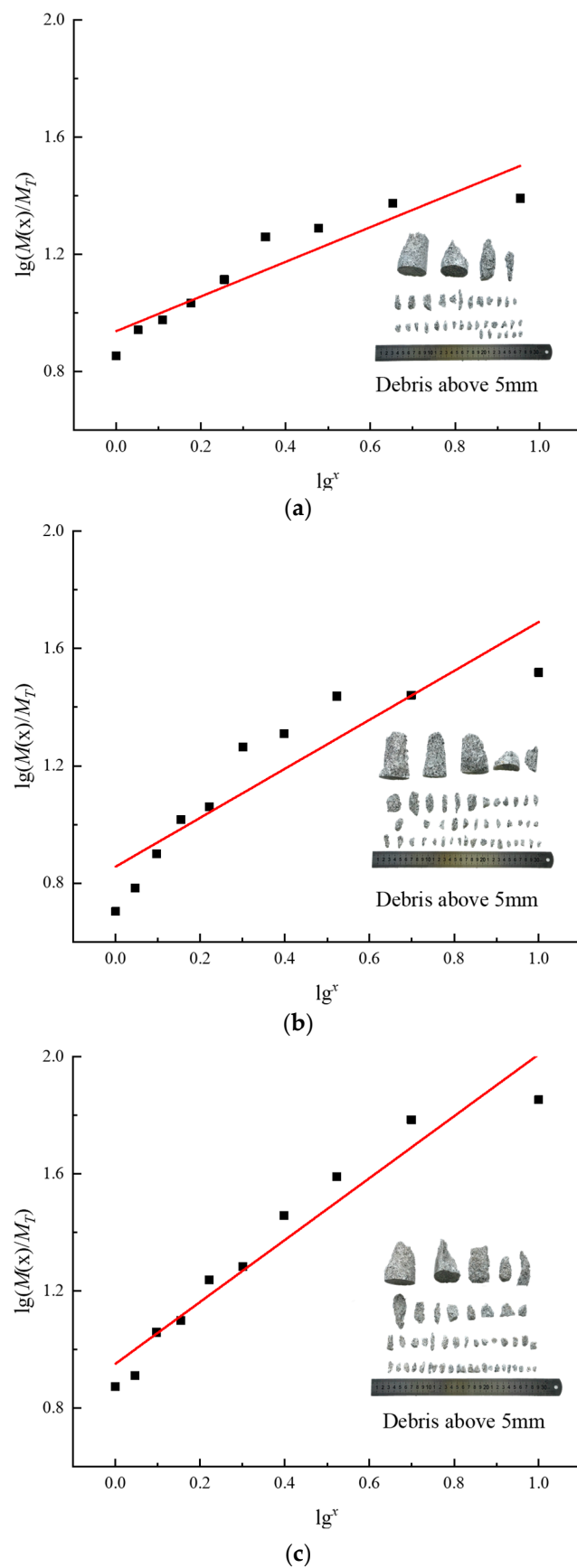


Figure 14. The $\lg(M(x)/M_T)$ – $\lg x$ lines of rocks under 70% of the UCS: (a) 20 MPa; (b) 30 MPa; (c) 40 MPa.

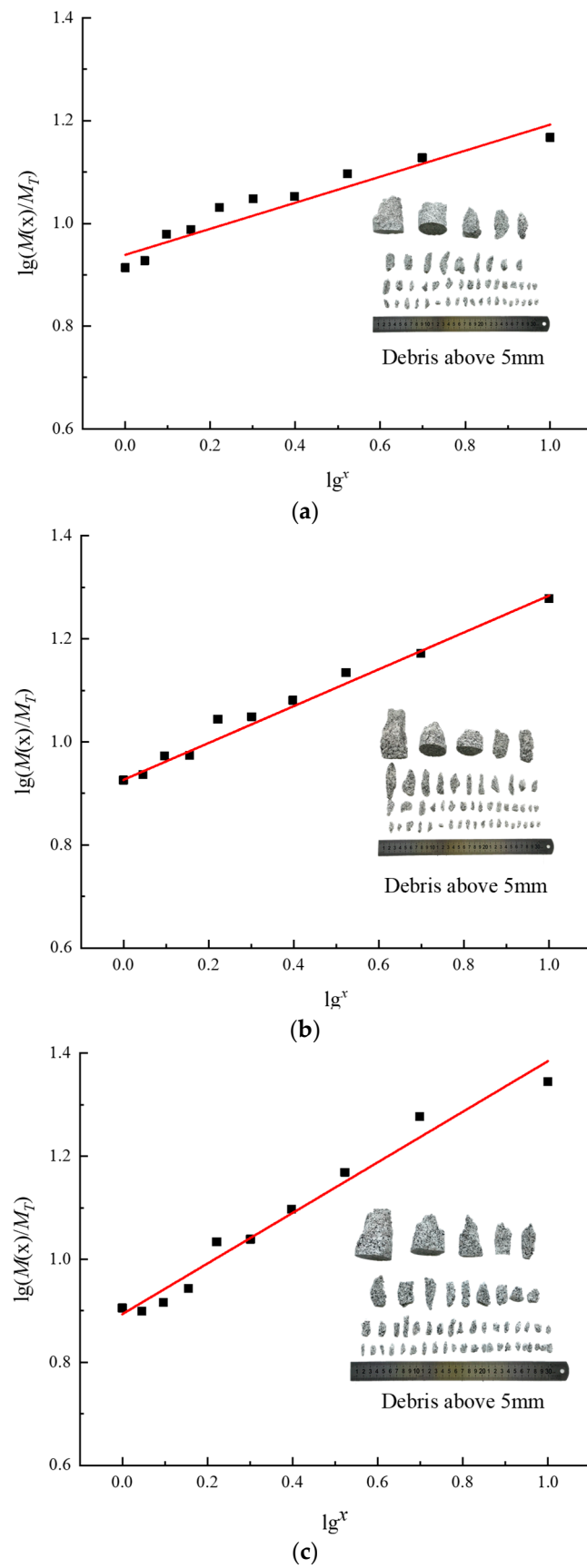


Figure 15. The $\lg(M(x)/M_T)$ – \log^x lines of rocks under 80% of the UCS: (a) 20 MPa; (b) 30 MPa; (c) 40 MPa.

3.2.3. Relationship between the Fractal Dimension and Amplitude of Disturbance

According to the slopes of the above $\log(M(x)/M_T)$ – $\log x$ fitted lines, the fractal dimensions F of each rock specimen are shown in Figure 16 (more detailed results are provided in Table 6): the correlation coefficients R^2 are all high, suggesting that the particle size distribution of rock fragments broken under the cyclic disturbance loads conforms to a fractal relationship. Under the same axial prestress σ_m , the rock specimens are found to have a fractal dimension F that increases with increasing amplitude of disturbance, reaching 2.4 at most; because the fractal dimension can be used to characterize the degree of fragmentation of rocks, the larger F is, the greater the degree of fragmentation of the rocks.

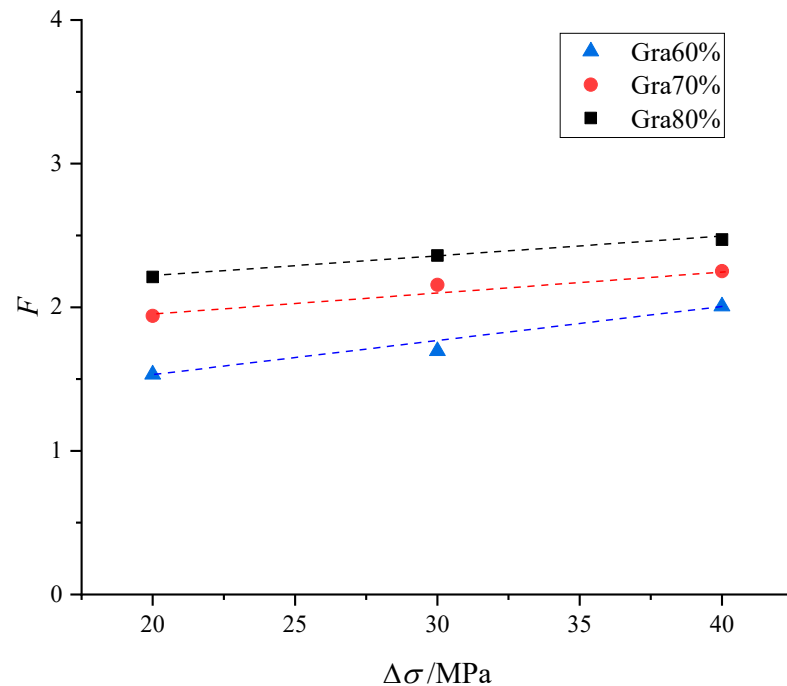


Figure 16. Evolution of the fractal dimension F .

Table 6. Statistical results: parameters of fragments of the granite.

Serial Number	F	R^2
Gra60%-1	1.5254	0.8746
Gra60%-2	1.7018	0.9043
Gra60%-3	2.0263	0.9459
Gra70%-1	1.9431	0.9401
Gra70%-2	2.1659	0.8549
Gra70%-3	2.2448	0.9045
Gra80%-1	2.2077	0.9682
Gra80%-2	2.3825	0.9615
Gra80%-3	2.4615	0.9099

3.3. Damage Analysis of Specimens under Disturbance Loads

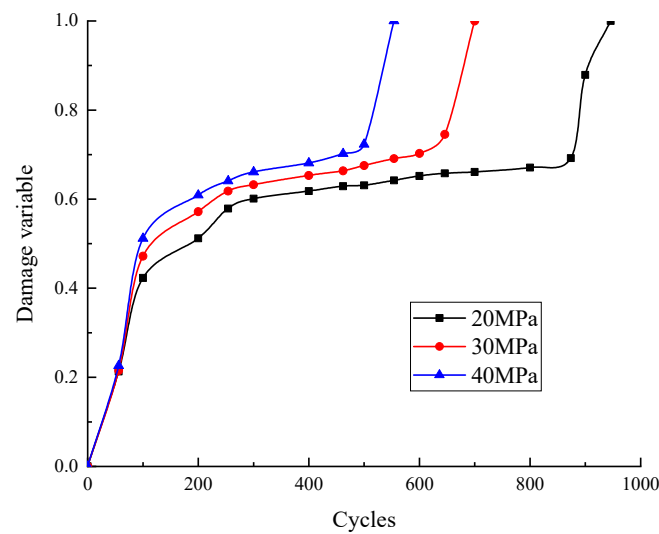
The failure of rocks under different cyclic dynamic disturbances is a gradual damage process of the internal part of rocks. The damage constitutive equation of rocks under the uniaxial compression is calculated as follows [14]:

$$\sigma = \varepsilon \times E \times (1 - D), \quad (7)$$

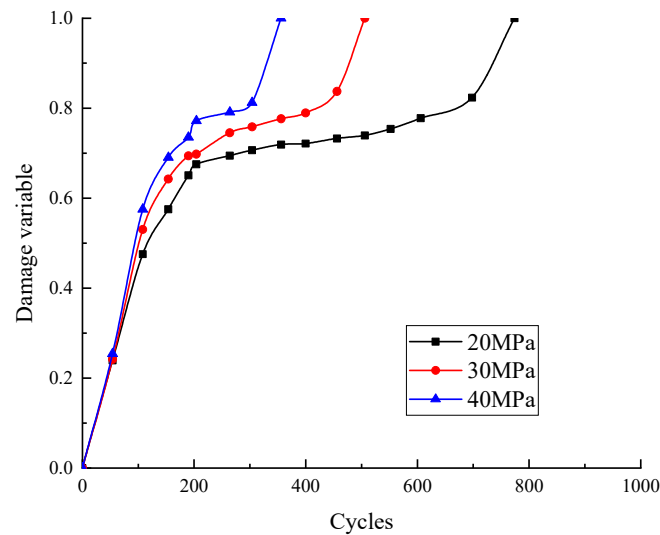
$$D = \frac{\varepsilon_d}{\varepsilon} \times \frac{\varepsilon - \varepsilon_0}{\varepsilon_0 \times \varepsilon_d}, \quad (8)$$

where σ , ε , E , and D separately represent the stress, strain, modulus of elasticity, and damage variable of rocks. The values of ε_0 and ε_d are derived according to the stress–strain curves in the test process.

Figure 17 shows the relationship between the number of disturbance cycles and the damage variable under different amplitudes of disturbance. The curves start from the axial static loading applied to the rock: the pre-set disturbance load is then applied until the rock specimen is damaged. It can be seen from the figure that the damage variable first shows a rapid, then steady, and, finally, rapidly increasing trend under the cyclic disturbance, and, as the amplitude of disturbance increases, the number of cycles in the steady increase stage is significantly reduced.



(a)



(b)

Figure 17. Cont.

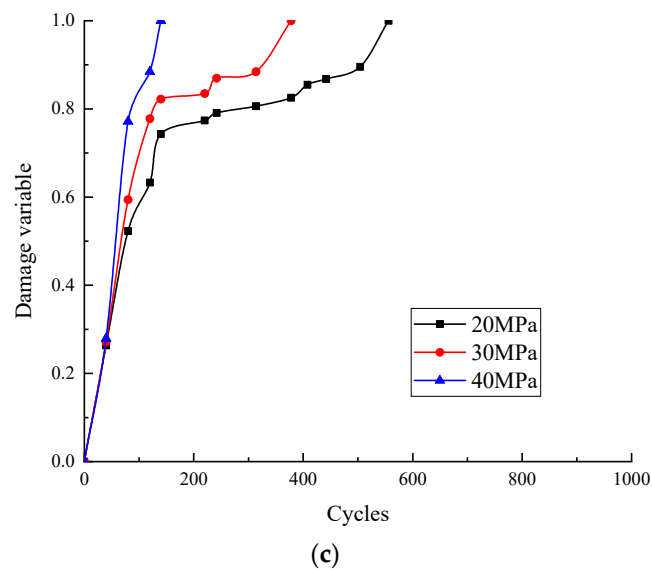


Figure 17. Relationship between the number of disturbance cycles and the damage variable: (a) 60%; (b) 70%; (c) 80%.

The rate of change of the damage variable in the steady increase stage is defined as V , which is calculated using the following formula [42]:

$$V = \frac{D_b - D_a}{C_b - C_a}, \quad (9)$$

where D_b and D_a are the initial damage variables in the steady increase stage; C_b and C_a represent the number of cycles of the initial disturbance loads that have been applied.

The rates of change of the damage variable in the steady increase stage, calculated using Formula (9), are shown in Figure 18 (more detailed results are provided in Table 7). It can be seen from Figure 18 that both the amplitude of disturbance loads, and the initial axial static loads exert significant influences on the rate of change of the damage variable in the steady increase stage. With the increasing amplitude of disturbance and the initial static load, the rate of change of the damage variable grows rapidly. Particularly when the initial static load is close to the peak strength, the rock shows a higher sensitivity to the disturbance, so that the rate of change of the damage variable rises significantly with the increasing amplitude of disturbance.

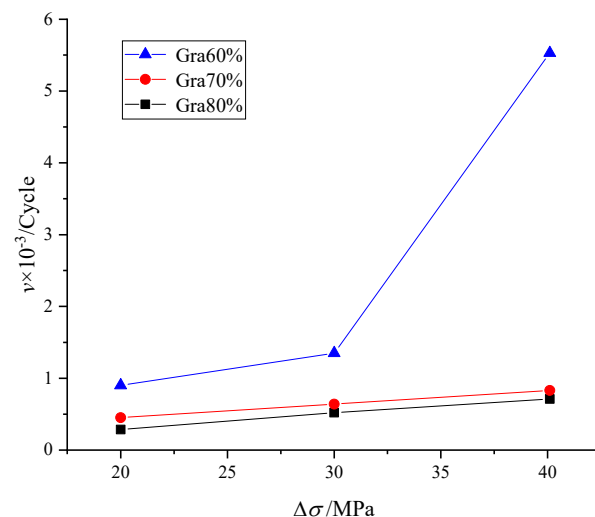


Figure 18. Rates of change of the damage variable of the rock in the steady increase stage.

Table 7. Rates of change of the damage variable.

Serial Number	Gra60%			Gra70%			Gra80%		
	1	2	3	1	2	3	1	2	3
$V \times 10^{-3}/\text{Cycle}$	0.28	0.56	0.76	0.46	0.62	0.81	0.89	1.34	5.5

4. Conclusions

Taking granite collected from the deep underground powerhouse of Shuangjiangkou Hydropower Station in Sichuan Province as the research object, mechanical tests were carried out on the rock under low-frequency cyclic disturbances. The characteristic stresses, fractal dimensions of fragments, and damage evolution of the deeply buried rock under disturbance environment were studied. The following conclusions were reached:

1. Under the dynamic disturbance loads, the failure stress of the granite under loading gradually increases with the increases in the initial prestress and the disturbance load due to the coupling between the damage and strain-rate effect. In the case that the initial axial prestress σ_m is the same, the failure stress shows an increasing trend with the increment in the amplitude of disturbance $\Delta\sigma$; under the same $\Delta\sigma$, the failure stress elevates with increasing σ_m .
2. The pre-peak section of the stress–strain curves during loading can be divided into four stages: initial crack compaction, elastic deformation, tensile crack development, and macro-crack development. The crack-closure stress, crack-initiation stress, and crack-damage stress are about 0.2, 0.4, and 0.7 times the peak stress, respectively. Under the disturbance loads, the characteristic stresses of the granite specimens increase with the growth of the amplitude of disturbance $\Delta\sigma$. Under the same $\Delta\sigma$, the characteristic stresses show an increasing trend with the increasing initial stress σ_m .
3. The particle size distribution of rock fragments broken under the disturbance loads follows a fractal relationship. Moreover, as the initial axial static load σ_m and the amplitude of disturbance $\Delta\sigma$ increase, the fractal dimension F rises, indicating a higher degree of fragmentation of the rock.
4. Damage to the rock specimens can be divided into rapid, steady, and rapid increase stages. As the amplitude of disturbance stress is increased, the number of cycles reduces remarkably in the steady increase stage, and the damage variable changes at a significantly increased rate. The rocks rapidly enter its final failure stage.

Author Contributions: B.F.: formal analysis, investigation, visualization; G.W.: conceptualization, methodology, writing—original draft, funding acquisition; X.L. (Xinping Li): writing—review and editing, supervision; X.L. (Xiqi Liu): writing—review and editing, funding acquisition; L.S.: writing—review and editing, funding acquisition. All authors have read and agreed to the published version of the manuscript.

Funding: The study was supported financially by the National Natural Science Foundation of China (No. 42002275), the National Natural Science Foundation of Zhejiang Province (No. LQ21D020001), the Collaborative Innovation Center for Prevention and Control of Mountain Geological Hazards of Zhejiang Province (No. PCMGH-2021-03), and the Hubei Key Laboratory of Roadway Bridge and Structure Engineering (Wuhan University of Technology) (No. DQJJ202104).

Institutional Review Board Statement: Not applicable.

Informed Consent Statement: Not applicable.

Data Availability Statement: Some or all data, models, or code that support the findings of this study are available from the corresponding author upon reasonable request.

Conflicts of Interest: The authors declare no conflict of interest.

References

1. Sidorov, D.V.; Potapchuk, M.I.; Sidlyar, A.V. Forecasting rock burst hazard of tectonically disturbed ore massif at the deep horizons of nikolaevskoe polymetallic deposit. *J. Min. Inst.* **2018**, *234*, 604–611. [\[CrossRef\]](#)
2. Khaledi, K.; Mahmoudi, E.; Datcheva, M.; Schanz, T. Stability and serviceability of underground energy storage caverns in rock salt subjected to mechanical cyclic loading. *Int. J. Rock Mech. Min.* **2016**, *86*, 115–131. [\[CrossRef\]](#)
3. Siwek, S. Earth tides and seismic activity in deep coal mining. *Int. J. Rock Mech. Min.* **2021**, *148*, 104972. [\[CrossRef\]](#)
4. Doğangün, A.; Ural, A.; Sezen, H.; Güney, Y.; Fırat, F.K. The 2011 earthquake in Simav, Turkey and seismic damage to reinforced concrete buildings. *Buildings* **2013**, *3*, 173–190. [\[CrossRef\]](#)
5. Gómez, S.; Sanchidrián, J.A.; Segarra, P. Near-field vibration from blasting and rock damage prediction with a full-field solution. *Int. J. Rock Mech. Min.* **2020**, *134*, 104357. [\[CrossRef\]](#)
6. Ma, C.S.; Chen, W.Z.; Tan, X.J.; Tian, H.M.; Yang, J.P.; Yu, J.X. Novel rockburst criterion based on the TBM tunnel construction of the Neelum–Jhelum (NJ) hydroelectric project in Pakistan. *Tunn. Undergr. Space Technol.* **2018**, *81*, 391–402. [\[CrossRef\]](#)
7. Sainoki, A.; Mitri, H.S. Dynamic behaviour of mining-induced fault slip. *Int. J. Rock Mech. Min.* **2014**, *66*, 19–29. [\[CrossRef\]](#)
8. Luo, Y.; Wang, G.; Li, X.; Liu, T.; Qu, D.; Huang, J. Research on triaxial compression failure characteristics and meso-simulation of brittle gypsum material. *Eur. J. Environ. Civ. Eng.* **2021**, *5*, 1–18. [\[CrossRef\]](#)
9. Mishra, S.; Chakraborty, T. Determination of high-strain-rate stress–strain response of granite for blast analysis of tunnels. *J. Eng. Mech.* **2019**, *145*, 04019057. [\[CrossRef\]](#)
10. Zhu, Y.; Yu, J.; Zhou, X.; Yang, Z.; Tang, X.; Liu, X. Uniaxial stress relaxation behavior of marble after cyclic disturbance loads. *Mech. Time-Depend. Mater.* **2021**, *25*, 513–537. [\[CrossRef\]](#)
11. Ghasemi, S.; Khomehchiyan, M.; Taheri, A.; Nikudel, M.R.; Zalooli, A. Microcracking behavior of gabbro during monotonic and cyclic loading. *Rock Mech. Rock Eng.* **2021**, *54*, 2441–2463. [\[CrossRef\]](#)
12. Cheng, Y.; Song, Z.; Song, W.; Li, S.; Yang, T.; Zhang, Z.; Wang, K. Strain performance and fracture response characteristics of hard rock under cyclic disturbance loading. *Geomech. Eng.* **2021**, *26*, 551–563. [\[CrossRef\]](#)
13. Wang, Y.; Li, C.H.; Liu, H.; Han, J.Q. Fracture failure analysis of freeze–thawed granite containing natural fracture under uniaxial multi-level cyclic loads. *Theor. Appl. Fract. Mech.* **2020**, *110*, 102782. [\[CrossRef\]](#)
14. Xu, T.; Fu, M.; Yang, S.Q.; Heap, M.J.; Zhou, G.L. A numerical meso-scale elasto-plastic damage model for modeling the deformation and fracturing of sandstone under cyclic loading. *Rock Mech. Rock Eng.* **2021**, *54*, 4569–4591. [\[CrossRef\]](#)
15. Manouchehrian, A.; Cai, M. Analysis of rockburst in tunnels subjected to static and dynamic loads. *J. Rock Mech. Geotech.* **2017**, *9*, 1031–1040. [\[CrossRef\]](#)
16. Yang, F.; Hu, D.; Zhou, H.; Lu, J. Physico-mechanical behaviors of granite under coupled static and dynamic cyclic loadings. *Rock Mech. Rock Eng.* **2020**, *53*, 2157–2173. [\[CrossRef\]](#)
17. Chen, X.; Tang, C.; Kong, X. Study on progressive damage and failure of sandstone samples subjected to cyclic disturbance loads using a modified triaxial test system. *KSCE J. Civ. Eng.* **2019**, *23*, 2371–2383. [\[CrossRef\]](#)
18. Su, G.; Hu, L.; Feng, X.; Wang, J.; Zhang, X. True triaxial experimental study of rockburst process under low frequency cyclic disturbance load combined with static load. *Chin. J. Rock Mech. Eng.* **2016**, *35*, 1309–1322. [\[CrossRef\]](#)
19. Delpueyo, D.; Balandraud, X.; Grédiac, M. Applying infrared thermography to analyse martensitic microstructures in a cu–al–be shape-memory alloy subjected to a cyclic loading. *Mater. Sci. Eng.* **2011**, *528*, 8249–8258. [\[CrossRef\]](#)
20. Kim, J.S.; Kim, G.Y.; Baik, M.H.; Finsterle, S.; Cho, G.C. A new approach for quantitative damage assessment of in situ rock mass by acoustic emission. *Geomech. Eng.* **2019**, *18*, 11–20. [\[CrossRef\]](#)
21. Li, X.; Chen, J.; Ma, C.; Huang, L.; Li, C.; Zhang, J.; Zhao, Y. A novel in-situ stress measurement method incorporating non-oriented core ground re-orientation and acoustic emission: A case study of a deep borehole. *Int. J. Rock Mech. Min.* **2022**, *152*, 105079. [\[CrossRef\]](#)
22. Shiotani, T.; Ohtsu, M.; Ikeda, K. Detection and evaluation of ae waves due to rock deformation. *Constr. Build. Mater.* **2001**, *15*, 235–246. [\[CrossRef\]](#)
23. Diaz, M.B.; Kim, K.Y.; Jung, S.G. Effect of frequency during cyclic hydraulic fracturing and the process of fracture development in laboratory experiments. *Int. J. Rock Mech. Min.* **2020**, *134*, 104474. [\[CrossRef\]](#)
24. Cai, M.; Morioka, H.; Kaiser, P.K.; Tasaka, Y.; Kurose, H.; Minami, M. Back-analysis of rock mass strength parameters using ae monitoring data. *Int. J. Rock Mech. Min.* **2007**, *44*, 538–549. [\[CrossRef\]](#)
25. Maji, V.; Murton, J.B. Experimental Observations and Statistical Modeling of Crack Propagation Dynamics in Limestone by Acoustic Emission Analysis During Freezing and Thawing. *J. Geophys. Res.-Earth.* **2021**, *126*, e2021JF006127. [\[CrossRef\]](#)
26. Young, R.P.; Nasser, M.; Sehzadeh, M. Mechanical and seismic anisotropy of rocks from the onkalo underground rock characterization facility. *Int. J. Rock Mech. Min.* **2020**, *126*, 104190. [\[CrossRef\]](#)
27. Mishra, S.; Khetwal, A.; Chakraborty, T. Dynamic characterisation of gneiss. *Rock Mech. Rock Eng.* **2019**, *52*, 61–81. [\[CrossRef\]](#)
28. Schmidt, F.; Menendez, J.; Konietzky, H.; Pascual-Muoz, P.; AB Sánchez. Converting closed mines into giant batteries: Effects of cyclic loading on the geomechanical performance of underground compressed air energy storage systems. *J. Energy Storage.* **2020**, *32*, 101882. [\[CrossRef\]](#)
29. Mansouri, H.; Ajalloeian, R. Mechanical behavior of salt rock under uniaxial compression and creep tests. *Int. J. Rock Mech. Min.* **2018**, *110*, 19–27. [\[CrossRef\]](#)

30. Liu, E.L.; He, S.; Xue, X.; Xu, J. Dynamic properties of intact rock samples subjected to cyclic loading under confining pressure conditions. *Rock Mech. Rock Eng.* **2011**, *44*, 629–634. [[CrossRef](#)]
31. Lu, G.M.; Zhou, J.; Zhang, B.; Pan, D.; Tong, T. Damage, deformation and energy characteristics of basalt after microwave irradiation subjected to cyclic loading. *Tunn. Constr.* **2020**, *40*, 1578–1585. [[CrossRef](#)]
32. Shi, H.; Song, L.; Zhang, H.; Xue, K.; Yuan, G.; Wang, Z.; Wang, G. Numerical study on mechanical and failure properties of sandstone based on the power-law distribution of pre-crack length. *Geomech. Eng.* **2019**, *19*, 421–434. [[CrossRef](#)]
33. Tho, V.D.; Korol, E.A.; Vatin, N.I.; Duc, H.M. The stress–strain state of three-layer precast flexural concrete enclosure structures with the contact interlayers. *Buildings*. **2021**, *11*, 88. [[CrossRef](#)]
34. Aashranth, B.; Davinci, M.A.; Samantaray, D.; Borah, U.; Albert, S.K. A new critical point on the stress-strain curve: Delineation of dynamic recrystallization from grain growth. *Mater. Des.* **2016**, *116*, 495–503. [[CrossRef](#)]
35. Cieřlik, J. Onset of crack initiation in uniaxial and triaxial compression tests of dolomite samples. *Stud. Geotech. Mech.* **2014**, *36*, 23–27. [[CrossRef](#)]
36. Cong, Y.; Cong, Y.; Zhang, L.; Jia, L.; Wang, Z. 3D particle flow simulation of loading-unloading failure process of marble. *Rock Soil Mech.* **2019**, *40*, 1179–1186. [[CrossRef](#)]
37. Song, L.; Wang, G.; Wang, X.; Huang, M.; Xu, K.; Han, G.; Liu, G. The influence of joint inclination and opening width on fracture characteristics of granite under triaxial compression. *Int. J. Geomech.* **2022**, *22*, 04022031. [[CrossRef](#)]
38. Baan, M.; Chorney, D. Insights from micromechanical modeling of intact rock failure: Event characteristics, stress drops, and force networks. *J. Geophys. Res.-Earth* **2019**, *124*, 12955–12980. [[CrossRef](#)]
39. Liu, L.; Li, H.; Li, X.; Wu, R. Full-field strain evolution and characteristic stress levels of rocks containing a single pre-existing flaw under uniaxial compression. *B Eng. Geol. Environ.* **2020**, *79*, 3145–3161. [[CrossRef](#)]
40. Su, G.; Chen, Z.; Jiang, J.; Mo, J.; Shi, Y. Experimental study on energy dissipating characteristics of rockburst fragments under different loading rates. *Chin. J. Geotech. Eng.* **2016**, *38*, 1481–1489. [[CrossRef](#)]
41. Odling, N.E. Natural fracture profiles, fractal dimension and joint roughness coefficients. *Rock Mech. Rock Eng.* **1994**, *27*, 135–153. [[CrossRef](#)]
42. Sirdesai, N.N.; Singh, A.; Sharma, L.K.; Singh, R.; Singh, T.N. Determination of thermal damage in rock specimen using intelligent techniques. *Eng. Geol.* **2018**, *239*, 179–194. [[CrossRef](#)]